Passive Imaging of Moving Targets with Sparsely Distributed Receivers

Ling Wang
College of Electronic and Information Engineering
Nanjing University of Aeronautics and Astronautics
Nanjing 210016, China
Email: wanglrpi@gmail.com

Birsen Yazıcı**
Department of Electrical, Computer and Systems Engineering,
Rensselaer Polytechnic Institute,
110 8th Street, Troy, NY 12180 USA
Email: yazici@ecse.rpi.edu

***Abstract*—We develop a novel passive image formation method for moving targets using measurements from a sparse array of receivers that rely on illumination sources of opportunity. We use a physics-based approach to model the wave propagation and develop a passive measurement model that expresses the measurement at each receiver in terms of the measurement at a different receiver. This model eliminates the need for knowledge about the transmitter locations and waveforms in the proposed image formation method. We formulate the image formation problem as a Generalized Likelihood Ratio Test (GLRT) for unknown target location and velocity using the proposed passive measurement model. We form the image in spatial and velocity space using the space- and velocity-resolved test-statistic. We present the resolution analysis of the imaging method using a moving point target model. We conduct numerical simulations to demonstrate the performance of the passive imaging algorithm.**

I. Introduction

With the rapid growth of broadcasting stations, mobile phone base stations, communication and navigation satellites, as well as relatively low cost and rapid deployment of receivers, passive radar imaging using transmitters of opportunity has emerged as an active area of research in recent years. A number of passive moving target detection and imaging approaches have been presented in the literature [1]–[10].

In this paper, we develop a novel passive image formation method for moving targets using static distributed receivers. The method is based on a new passive measurement model and a space- and velocity-resolved binary hypothesis testing. As compared to the existing methods [1]–[10], our approach determines the two- or three-dimensional velocity information as well as two- or three-dimensional position of targets and requires no information on the location of transmitters or the transmitted waveforms. Additionally, it does not rely on receivers with high directivity.

II. Passive Measurement Model

For a single transmitter with isotropic antenna located at $\mathbf{z}$ transmitting the waveform $p(t)$ starting at time $t = -T_{\mathbf{z}}$, the propagation of electromagnetic waves in a medium can be described using the scalar wave equation,

$$[\nabla^2 - c^{-2}(t,\mathbf{x})\partial_t^2]E(t,\mathbf{x},\mathbf{z}) = \delta(\mathbf{x}-\mathbf{z})p(t+T_{\mathbf{z}}) \quad (1)$$

where c is the wave speed in the medium and E is the electric field. Note that this model can be extended to realistic antenna models and multiple transmitters in a straightforward manner.

A single scatterer moving at velocity $\mathbf{v}$ corresponds to an index-of-refraction distribution $n^2(\mathbf{x}-\mathbf{v}t)$. Thus, the wave speed c can be expressed as

$$c^{-2}(t,\mathbf{x}) = c_0^{-2}[1 + n^2(\mathbf{x}-\mathbf{v}t)] \quad (2)$$

where c_0 denotes the speed in the background medium and the second term in (2) represents the perturbation due to deviation from the background reflectivity that is caused by the moving scatterer. In this work, we focus specially on radar imaging and assume that c_0 is equal to the speed of light in vacuum.

Let $q_{\mathbf{v}}(\mathbf{x}-\mathbf{v}t) = c_0^{-2}n^2(\mathbf{x}-\mathbf{v}t)$. The moving scatterers in the spatial volume d^3x centered at $\mathbf{x}$ give rise to $c^{-2}(t,\mathbf{x}) = c_0^{-2} + \int q_{\mathbf{v}}(\mathbf{x}-\mathbf{v}t)d^3v$ [11].

The propagation medium is characterized by the *Green's function*. For free-space, the *Green's function* is given by

$$g(\mathbf{x},\mathbf{z},t) = \frac{\delta(t-|\mathbf{x}-\mathbf{z}|/c_0)}{4\pi|\mathbf{x}-\mathbf{z}|}. \quad (3)$$

We assume that the electromagnetic waves decay rapidly as they penetrate the ground. We then write $q_{\mathbf{v}}(\mathbf{x}-\mathbf{v}t)$ in terms of 2D location and 2D velocity as in

$$q_{\mathbf{v}}(\mathbf{x}-\mathbf{v}t) = q_{\boldsymbol{v}}(\boldsymbol{x}-\boldsymbol{v}t)\delta(x_3 - h(\boldsymbol{x}))\delta(v_3 - D\cdot\boldsymbol{v}) \quad (4)$$

where $\mathbf{x} = (\boldsymbol{x}, x_3), \boldsymbol{x} \in \mathbb{R}^2$ and $\mathbf{v} = (\boldsymbol{v}, v_3), \boldsymbol{v} \in \mathbb{R}^2$, h represents the ground topography and $D = [\frac{\partial h}{\partial x_1} \quad \frac{\partial h}{\partial x_2}]$.

For the slow-mover case where the speed of the target is much slower than the speed of light c_0, the scattered field measurement at the receiver located at $\mathbf{x}_0$ due to a transmitter located at $\mathbf{z}$ is expressed as [11]

$$m(t) = \int \frac{\ddot{p}\left[\alpha_{\boldsymbol{y},\boldsymbol{v},\mathbf{x}_0,\mathbf{z}}\left(t-|\mathbf{y}-\mathbf{x}_0|/c_0\right) - |\mathbf{y}-\mathbf{z}|/c_0 + T_{\mathbf{z}}\right]}{(4\pi)^2|\mathbf{y}-\mathbf{x}_0||\mathbf{y}-\mathbf{z}|} \times q_{\boldsymbol{v}}(\boldsymbol{y})d\boldsymbol{y}d\boldsymbol{v} + n(t) \quad (5)$$

This work was supported by the Air Force Office of Scientific Research (AFOSR) under the agreements FA9550-07-1-0363 and FA9550-09-1-0013 and National Science Foundation (NSF) under Grant No. CCF-08030672.

** Corresponding author

where

$$\alpha_{\boldsymbol{y},\boldsymbol{v},\mathbf{x}_0,\mathbf{z}} = \frac{1 - \widehat{\mathbf{y}-\mathbf{z}} \cdot \mathbf{v}/c_0}{1 + \widehat{\mathbf{y}-\mathbf{x}_0} \cdot \mathbf{v}/c_0} \tag{6}$$

is the *Doppler-scale-factor* [11] and $n(t)$ is the additive thermal noise at the receiver. Note that $\mathbf{y} = (\boldsymbol{y}, h(\boldsymbol{y}))$ and $\mathbf{v} = (\boldsymbol{v}, D \cdot \boldsymbol{v})$. In Fourier domain, (5) becomes

$$\hat{m}(\omega) = \frac{-\omega^2}{(4\pi)^2} \int \frac{\mathrm{e}^{\mathrm{i}\phi_{\boldsymbol{y},\boldsymbol{v},\mathbf{x}_0}}}{|\mathbf{y}-\mathbf{x}_0||\mathbf{y}-\mathbf{z}|\alpha^3_{\boldsymbol{y},\boldsymbol{v},\mathbf{x}_0,\mathbf{z}}} \hat{p}\left(\frac{\omega}{\alpha_{\boldsymbol{y},\boldsymbol{v},\mathbf{x}_0,\mathbf{z}}}\right) \times q_{\boldsymbol{v}}(\boldsymbol{y}) d\boldsymbol{y} d\boldsymbol{v} + \hat{n}(\omega). \tag{7}$$

where

$$\phi = \frac{\omega}{\alpha_{\boldsymbol{y},\boldsymbol{v},\mathbf{x}_0,\mathbf{z}}} \left(T_{\mathbf{z}} - \frac{|\mathbf{y}-\mathbf{z}|}{c_0}\right) - \omega \frac{|\mathbf{y}-\mathbf{x}_0|}{c_0}. \tag{8}$$

In the analysis that follows, we consider a sparse distribution of N receivers located at $\mathbf{x}_i, i = 1, \cdots, N$. We assume that there is a single transmitter located at $\mathbf{z}_0$ transmitting waveform p_0 starting at time $t = -T_0$. This assumption allows us to simplify the analysis and distill the important aspects of our imaging theory. The results obtained in this paper can easily be extended to multiple-transmitter case.

Passive measurement model cannot depend on the transmitter location or transmitted waveforms. We develop an alternative measurement model that expresses measurements at each receiver in terms of the measurements at a different receiver, which involves a back-propagation operation and a forward-propagation operation.

Let $u = -q_{\boldsymbol{v}}(\boldsymbol{y})\omega^2 \hat{E}^{\mathrm{in}}(\boldsymbol{y}, \boldsymbol{v}, \omega)$ where

$$\tilde{\hat{E}}^{\mathrm{in}}(\boldsymbol{y}, \boldsymbol{v}, \omega) = \frac{\mathrm{e}^{\mathrm{i}\frac{\omega}{\tilde{\mu}_{\boldsymbol{y},\boldsymbol{v},\mathbf{z}_0}}\left(T_0 - \frac{|\mathbf{y}-\mathbf{z}_0|}{c_0}\right)}}{4\pi|\mathbf{y}-\mathbf{z}_0|\tilde{\mu}_{\boldsymbol{y},\boldsymbol{v},\mathbf{z}_0}} \hat{p}_0\left(\frac{\omega}{\tilde{\mu}_{\boldsymbol{y},\boldsymbol{v},\mathbf{z}_0}}\right) \tag{9}$$

with $\tilde{\mu}_{\boldsymbol{y},\boldsymbol{v},\mathbf{z}_0} = 1 - \widehat{\mathbf{y}-\mathbf{z}_0} \cdot \mathbf{v}/c_0$. Note that $\tilde{\hat{E}}^{\mathrm{in}}$ can be viewed as the incident field observed by a moving target. The scale factor, $\tilde{\mu}$, accounts for the Doppler scaling effect induced by the movement of the target on the field due to the transmitted waveform.

Let $\hat{m}_i$ denote the Fourier transform of the measurement at the i^{th} receiver. Using (7), we define the linear operator, $\mathcal{P}_{\boldsymbol{y},\boldsymbol{v},i}$, that propagates the field u to the i^{th} measurements, i.e.,

$$\mathcal{P}_{\boldsymbol{y},\boldsymbol{v},i}[u](\omega) \quad = \hat{m}_j(\omega) \tag{10}$$

as the forward-propagation operator with respect to the i^{th} receiver. Using (7), we express $\mathcal{P}_{\boldsymbol{y},\boldsymbol{v},i}$ as follows:

$$\mathcal{P}_{\boldsymbol{y},\boldsymbol{v},i}[u](\omega) \quad = \mathcal{G}_{\boldsymbol{y},i}\mathcal{S}_{\boldsymbol{v},i}[u](\omega). \tag{11}$$

where $\mathcal{S}_{\boldsymbol{v},i}$ is a scaling operator that accounts for the Doppler-scale factor observed by the i^{th} receiver due to the movement of the target at the hypothetical velocity $\boldsymbol{v}$; and $\mathcal{G}_{\boldsymbol{y},i}$ in (11) is a propagation operator that accounts for the time delay from the target to the i^{th} receiver in free-space.

$\mathcal{S}_{\boldsymbol{v},i}$ is given by

$$\mathcal{S}_{\boldsymbol{v},i}[u](\omega) = \int W_v(\boldsymbol{v}', \boldsymbol{v}) \mu_{\boldsymbol{y},\boldsymbol{v}',i}\, u(\mu_{\boldsymbol{y},\boldsymbol{v}',i}\,\omega) d\boldsymbol{v}' \tag{12}$$

where $W_v(\boldsymbol{v}', \boldsymbol{v})$ is a windowing function of unit amplitude in velocity space centered at the hypothetical velocity $\boldsymbol{v}$ and

$$\mu_{\boldsymbol{y},\boldsymbol{v},i} = 1 + \widehat{\mathbf{y}-\mathbf{x}_i} \cdot \mathbf{v}/c_0, \tag{13}$$

which accounts for the Doppler-scale-factor observed by the i^{th} receiver due to the movement of the target at the hypothetical velocity $\boldsymbol{v}$.

$\mathcal{G}_{\boldsymbol{y},i}$ in (11) is given by

$$\mathcal{G}_{\boldsymbol{y},i}[u](\omega) = \int W_s(\boldsymbol{y}', \boldsymbol{y}) \hat{g}(\mathbf{x}_i, \boldsymbol{y}, \omega) u(\boldsymbol{y}', \boldsymbol{v}, \omega) d\boldsymbol{y}' \tag{14}$$

where $W_s(\boldsymbol{y}', \boldsymbol{y})$ is a spatial windowing function of unit amplitude centered at a hypothetical target location $\boldsymbol{y}$ and $\hat{g}(\mathbf{x}_i, \boldsymbol{y}, \omega)$ represents the Fourier transform of (3).

We define the back-propagation operator as the inverse of $\mathcal{P}_{\boldsymbol{y},\boldsymbol{v},i}$ and denote it by $\mathcal{P}^{-1}_{\boldsymbol{y},\boldsymbol{v},i}$. Using (11), we obtain

$$\mathcal{P}^{-1}_{\boldsymbol{y},\boldsymbol{v},i}[\hat{m}_i](\omega) = \mathcal{S}^{-1}_{\boldsymbol{v},i}\mathcal{G}^{-1}_{\boldsymbol{y},i}[\hat{m}_i](\omega) \tag{15}$$

where $\mathcal{G}^{-1}_{\boldsymbol{y},i}$ is the inverse of $\mathcal{G}_{\boldsymbol{y},i}$, $\mathcal{S}^{-1}_{\boldsymbol{v},i}$ is the inverse of $\mathcal{S}_{\boldsymbol{v},i}$ and $\hat{m}_i$ represents the measurement at the i^{th} receiver. Note that if $\mathcal{P}^{-1}_{\boldsymbol{y},\boldsymbol{v},i}$ does not exist, it may be replaced with its pseudoinverse.

We now express the measurement at the i^{th} receiver, $\hat{m}_i$ in terms of the measurement at the j^{th} receiver, $\hat{m}_j$, by back-propagating $\hat{m}_j$ measured at $\mathbf{x}_j$ to a hypothetical target location with a hypothetical velocity via the back-propagation operator and then forward-propagating the resulting field to $\mathbf{x}_i$ via the forward-propagation operator. Let $\hat{m}^j_i(\omega)$ denote the i^{th} measurement expressed in terms of the j^{th} measurement. We define the passive measurement model for the j^{th} measurement as follows:

$$\hat{m}^j_i(\omega) = \mathcal{P}_{\boldsymbol{y},\boldsymbol{v},i}\mathcal{P}^{-1}_{\boldsymbol{y},\boldsymbol{v},j}\hat{m}_j(\omega) + \hat{n}_i(\omega) \tag{16}$$

where $\hat{n}_i(\omega)$ is the additive thermal noise at the i^{th} receiver.

Taking the j^{th} receiver as a reference, we form the following measurement vector for N receivers:

$$\mathbf{m} = \left[\begin{array}{cccc} \hat{m}^j_1 & \hat{m}^j_2 & \cdots & \hat{m}^j_N \end{array}\right]^T \tag{17}$$

where $\hat{m}^j_i$, $i = 1, \cdots, N$ and $i \neq j$, denotes the measurement $\hat{m}_i$ modeled in terms of the reference measurement $\hat{m}_j$. Similarly, we vectorize the "reference measurements", $\hat{m}_j$'s, and the noise:

$$\mathbf{m_r} = \left[\begin{array}{cccc} \hat{m}_j & \hat{m}_j & \cdots & \hat{m}_j \end{array}\right]^T \tag{18}$$

$$\mathbf{n} = \left[\begin{array}{cccc} \hat{n}_1 & \hat{n}_2 & \cdots & \hat{n}_N \end{array}\right]^T. \tag{19}$$

Note that $\mathbf{m}, \mathbf{m_r}$ and $\mathbf{n}$ are all $(N-1)$ vectors.

We represent the composition of the back-propagation and forward-propagation operators as a diagonal matrix as follows:

$$\mathbf{P}_{\boldsymbol{y},\boldsymbol{v}} = \mathrm{diag}\left[\begin{array}{cccc} \mathcal{P}_{\boldsymbol{y},\boldsymbol{v},1}\mathcal{P}^{-1}_{\boldsymbol{y},\boldsymbol{v},j} & \cdots & \mathcal{P}_{\boldsymbol{y},\boldsymbol{v},N}\mathcal{P}^{-1}_{\boldsymbol{y},\boldsymbol{v},j} \end{array}\right] \tag{20}$$

where $i \neq j$ and $\mathbf{P}_{\boldsymbol{y},\boldsymbol{v}}$ is $(N-1) \times (N-1)$.

Using (16), (17)-(20), we form the vectorized passive measurement model as follows:

$$\mathbf{m}(\omega) = \mathbf{P}_{\boldsymbol{y},\boldsymbol{v}}\mathbf{m_r}(\omega) + \mathbf{n}(\omega) \tag{21}$$

for some range of ω.

Note that in (21) all the operations are understood to be elementwise.

III. Image Formation in Spatial and Velocity Space

We formulate the image formation problem as a test of binary hypothesis, which has its roots in the Generalized Likelihood Ratio Test (GLRT) [12]. We extract a space- and velocity-resolved test-statistic as opposed to reconstructing the unknown quantities of interest themselves due to the limited number of measurements available. The image is then formed in $(\boldsymbol{y}, \boldsymbol{v})$ domain by the space- and velocity-resolved test-statistic where the location and the velocity can be identified by thresholding the image.

We define the space- and velocity-resolved binary hypothesis test as follows:

$$\begin{array}{ll} \mathcal{H}_0: & \mathbf{m} = \mathbf{n} \\ \mathcal{H}_1: & \mathbf{m} = \mathbf{P}_{\boldsymbol{y},\boldsymbol{v}}\mathbf{m}_{\mathbf{r}} + \mathbf{n} \end{array} \tag{22}$$

where $\mathbf{P}_{\boldsymbol{y},\boldsymbol{v}}, \mathbf{m}_r, \mathbf{m}$ and $\mathbf{n}$ are as defined in (17)-(21). The null hypothesis states that the measurement is due to noise whereas the alternative hypothesis states that the measurement is due to a target located at $\boldsymbol{y}$ moving with velocity $\boldsymbol{v}$.

Using (16), (18), (19) and (22), we obtain

$$\mathrm{E}\left[\mathbf{m}|\mathcal{H}_0\right] = \mathbf{0} \tag{23}$$

$$\mathrm{Cov}\left[\mathbf{m}|\mathcal{H}_0\right] = \mathbf{R}_{\mathbf{n}} =: \mathbf{R}_0 \tag{24}$$

$$\mathrm{E}\left[\mathbf{m}|\mathcal{H}_1\right] = \mathbf{P}_{\boldsymbol{y},\boldsymbol{v}}\mathrm{E}\left[\mathbf{m}_{\mathbf{r}}|\mathcal{H}_1\right] = \mathbf{P}_{\boldsymbol{y},\boldsymbol{v}}\overline{\mathbf{m}}_{\mathbf{r}} \tag{25}$$

$$\mathrm{Cov}\left[\mathbf{m}|\mathcal{H}_1\right] = \mathbf{P}_{\boldsymbol{y},\boldsymbol{v}}\mathbf{R}_{\mathbf{n}_{\mathbf{r}}}\mathbf{P}^H_{\boldsymbol{y},\boldsymbol{v}} + \mathbf{R}_{\mathbf{n}} =: \mathbf{R}_1 \tag{26}$$

where $\mathrm{E}\left[\cdot\right]$ denotes the expectation operator and $\mathrm{Cov}\left[\cdot\right]$ denotes the covariance operator, $\overline{\mathbf{m}}_{\mathbf{r}}$ denotes $\mathrm{E}\left[\mathbf{m}_{\mathbf{r}}|\mathcal{H}_1\right]$, $\mathbf{P}^H_{\boldsymbol{y},\boldsymbol{v}}$ denotes the Hermitian transpose of $\mathbf{P}_{\boldsymbol{y},\boldsymbol{v}}$, $\mathbf{R}_{\mathbf{n}}$ denotes the autocovariance of the vector $\mathbf{n}$, i.e., $\mathbf{R}_{\mathbf{n}}(\omega,\omega') = \mathrm{E}\left[\mathbf{n}(\omega)\mathbf{n}^H(\omega')\right]$ and $\mathbf{R}_{\mathbf{n}_{\mathbf{r}}}$ is the autocovariance of the noise vector $\mathbf{n}_{\mathbf{r}} = [\hat{n}_j, \hat{n}_j, \cdots, \hat{n}_j]$, i.e., $\mathbf{R}_{\mathbf{n}_{\mathbf{r}}}(\omega,\omega') = \mathrm{E}\left[\mathbf{n}_{\mathbf{r}}(\omega)\mathbf{n}^H_{\mathbf{r}}(\omega')\right]$.

We determine the test-statistic by maximizing the signal-to-noise ratio (SNR) of the test-statistic while constraining the associated discriminant functional to be linear. The linear discriminant functional involved in our problem has the form

$$\lambda = \langle \mathbf{m}, \mathbf{w} \rangle := \int \mathbf{w}^H \mathbf{m} d\omega = \sum_{i \neq j} \int w_i^*(\omega)\hat{m}_i^j(\omega) d\omega \tag{27}$$

where λ denote the the output of the discriminant functional, which we call the *test-statistic* and $\mathbf{w}$ is a template given by $\mathbf{w} = [w_1 \quad w_2 \cdots w_N]^T$.

Under the assumption that the noise at different receivers are wide sense stationary and mutually uncorrelated, the maximization of the SNR of λ [12] results in an optimal linear template given by

$$\mathbf{w}^\star = \overline{\mathbf{S}}^{-1}(\omega)\mathbf{P}_{\boldsymbol{y},\boldsymbol{v}}(\omega)\overline{\mathbf{m}}_{\mathbf{r}}(\omega) \tag{28}$$

where $\overline{\mathbf{S}}^{-1}$ is the inverse of $\overline{\mathbf{S}}$ defined by $\overline{\mathbf{S}}(\omega) = \int 1/2(\mathbf{R}_1(\omega,\omega') + \mathbf{R}_0(\omega,\omega'))d\omega'$. Using (24) and (26), We can approximate $\overline{\mathbf{S}}^{-1}$ by a diagonal matrix. (See [**?**] for details.) We denote diagonal elements of $\overline{\mathbf{S}}^{-1}$ by $\overline{S}_i^{-1}(\omega), i = 1, \cdots, N$ and $i \neq j$, which is a function of the power spectral density function of noise at the i^{th} receiver and the kernel of $\mathbf{P}_{\boldsymbol{y},\boldsymbol{v}}$.

IV. Resolution Analysis

In this section, we assume that the surface topography is flat, i.e., $h(\boldsymbol{y}) = h$, for some $\boldsymbol{y} \in \mathbb{R}^2$ and therefore set $\mathbf{y} = [\boldsymbol{y}, h]$, $\mathbf{v} = [\boldsymbol{v}, 0]$. We focus our analysis on the deterministic moving point target model given by

$$q_{\boldsymbol{v}}(\boldsymbol{y}) = T\delta(\boldsymbol{y} - \boldsymbol{y}_0)\delta(\boldsymbol{v} - \boldsymbol{v}_0) \tag{29}$$

and analyze how moving point targets are resolved in the four-dimensional image $\lambda(\boldsymbol{y},\boldsymbol{v}), \boldsymbol{y}, \boldsymbol{v} \in \mathbb{R}^2$.

Let $K(\boldsymbol{y}, \boldsymbol{y}_0; \boldsymbol{v}, \boldsymbol{v}_0)$ denote the PSF of the four-dimensional imaging operator. We define K as the expected value of the image of a moving point target represented by (29), i.e., $K(\boldsymbol{y}, \boldsymbol{y}_0; \boldsymbol{v}, \boldsymbol{v}_0) := \mathrm{E}\left[\lambda(\boldsymbol{y},\boldsymbol{v})\right]$. For a deterministic moving point target model given by (29), we have

$$\mathrm{E}\left[\hat{m}_j(\omega)\right] = \frac{\omega^2 T \mathrm{e}^{\mathrm{i}\phi_{\boldsymbol{y}_0,\boldsymbol{v}_0,\mathrm{j}}}}{(4\pi)^2|\mathbf{y}_0 - \mathbf{x}_j||\mathbf{y}_0 - \mathbf{z}_0|\alpha^3_{\boldsymbol{y}_0,\boldsymbol{v}_0,\mathbf{x}_j,\mathbf{z}_0}} \times \hat{p}_0\left(\frac{\omega}{\alpha_{\boldsymbol{y}_0,\boldsymbol{v}_0,\mathbf{x}_j,\mathbf{z}_0}}\right) \tag{30}$$

where $\alpha_{\boldsymbol{y}_0,\boldsymbol{v}_0,\mathbf{x}_j,\mathbf{z}_0}$ is as described by (6) and

$$\phi_{\boldsymbol{y}_0,\boldsymbol{v}_0,j} = \frac{\omega}{\alpha_{\boldsymbol{y}_0,\boldsymbol{v}_0,\mathbf{x}_j,\mathbf{z}_0}}\left(T_{\mathbf{z}_1} - \frac{|\mathbf{y}_0 - \mathbf{z}_0|}{c_0}\right) - \omega\frac{|\mathbf{y}_0 - \mathbf{x}_j|}{c_0}. \tag{31}$$

For notational simplicity, we drop $\mathbf{z}_0$ from the subscript of α for the rest of our paper.

We assume that there are two receivers located at $\mathbf{x}_1$ and $\mathbf{x}_2$ and take the measurement at the $\mathbf{x}_1$ as the reference. Thus, using (27), (28), (11), (15), (12), (14) and (29), we have

$$K(\boldsymbol{y}, \boldsymbol{y}_0; \boldsymbol{v}, \boldsymbol{v}_0) = \frac{|\mathbf{y} - \mathbf{x}_1|}{|\mathbf{y} - \mathbf{x}_2|}\gamma_{\boldsymbol{y},\boldsymbol{v},21}\int \overline{S}_2^{-1}(\omega) \times \mathrm{e}^{-\mathrm{i}k\left(|\mathbf{y}-\mathbf{x}_2| - \gamma_{\boldsymbol{y},\boldsymbol{v},21}|\mathbf{y}-\mathbf{x}_1|\right)}\mathrm{E}\left[\hat{m}_1(\gamma_{\boldsymbol{y},\boldsymbol{v},21}\,\omega)\right]\mathrm{E}\left[\hat{m}_2^*(\omega)\right] d\omega \tag{32}$$

where

$$\gamma_{\boldsymbol{y},\boldsymbol{v},21} = \frac{1 + \widehat{\mathbf{y} - \mathbf{x}_2} \cdot \mathbf{v}/c_0}{1 + \widehat{\mathbf{y} - \mathbf{x}_1} \cdot \mathbf{v}/c_0}. \tag{33}$$

Using (30), (32) becomes

$$K(\boldsymbol{y}, \boldsymbol{y}_0; \boldsymbol{v}, \boldsymbol{v}_0) = \beta\int \overline{S}_2^{-1}(\omega)\omega^4 \mathrm{e}^{-\mathrm{i}\,\mathrm{k}r_{21}} \times \mathrm{e}^{\mathrm{i}k\left[\left(\frac{\gamma_{\boldsymbol{y},\boldsymbol{v},21}}{\alpha_{\boldsymbol{y}_0,\boldsymbol{v}_0,\mathbf{x}_1}} - \frac{1}{\alpha_{\boldsymbol{y}_0,\boldsymbol{v}_0,\mathbf{x}_2}}\right)\left(cT_{\mathbf{z}_0} - |\mathbf{y}_0 - \mathbf{z}_0|\right)\right]} \times \hat{p}_0\left(\frac{\gamma_{\boldsymbol{y},\boldsymbol{v},21}}{\alpha_{\boldsymbol{y}_0,\boldsymbol{v}_0,\mathbf{x}_1}}\omega\right)\hat{p}_0^*\left(\frac{\omega}{\alpha_{\boldsymbol{y}_0,\boldsymbol{v}_0,\mathbf{x}_2}}\right) d\omega \tag{34}$$

where β is a s scaling term due to geometric spreading factors and Doppler-scale-factors and

$$r_{21} = |\mathbf{y} - \mathbf{x}_2| - \gamma_{\boldsymbol{y},\boldsymbol{v},21}|\mathbf{y} - \mathbf{x}_1| - \left(|\mathbf{y}_0 - \mathbf{x}_2| - \gamma_{\boldsymbol{y},\boldsymbol{v},21}|\mathbf{y}_0 - \mathbf{x}_1|\right). \tag{35}$$

Examining (34), we see that if

$$\frac{\gamma_{\boldsymbol{y},\boldsymbol{v},21}}{\alpha_{\boldsymbol{y}_0,\boldsymbol{v}_0,\mathbf{x}_1}} = \frac{1}{\alpha_{\boldsymbol{y}_0,\boldsymbol{v}_0,\mathbf{x}_2}}, \tag{36}$$

(34) becomes

$$K(\boldsymbol{y},\boldsymbol{y}_0;\boldsymbol{v},\boldsymbol{v}_0)=\frac{T^2|\mathbf{y}-\mathbf{x}_1|}{(4\pi)^4|\mathbf{y}_0-\mathbf{z}_0|^2|\mathbf{y}_0-\mathbf{x}_1||\mathbf{y}-\mathbf{x}_2|\alpha^6_{\boldsymbol{y}_0,\boldsymbol{v}_0,\mathbf{x}_2}} \times\int\overline{S}_2^{-1}(\omega)\omega^4\mathrm{e}^{-\mathrm{i}\,kr_{21}}\left|\hat{p}_0\left(\frac{\omega}{\alpha_{\boldsymbol{y}_0,\boldsymbol{v}_0,\mathbf{x}_2}}\right)\right|^2 d\omega \quad (37)$$

which defines the correlation of $\left|\overline{S}_2^{-1/2}(\omega)\omega^2\hat{p}_1\left(\frac{\omega}{\alpha_{\boldsymbol{y}_0,\boldsymbol{v}_0,\mathbf{x}_2}}\right)\right|$ with itself in time domain. Clearly, this correlation peaks when $r_{21}=0$, i.e.,

$$|\mathbf{y}-\mathbf{x}_2|-\gamma_{\boldsymbol{y},\boldsymbol{v},21}|\mathbf{y}-\mathbf{x}_1|=|\mathbf{y}_0-\mathbf{x}_2|-\gamma_{\boldsymbol{y},\boldsymbol{v},21}|\mathbf{y}_0-\mathbf{x}_1|\,. \quad (38)$$

The analysis above shows that the PSF of the imaging operator for two receivers and one transmitter becomes maximum under the two conditions given by (36) and (38).

Substituting (6) into (36), we have

$$\gamma_{\boldsymbol{y},\boldsymbol{v},21}=\frac{1+\widehat{\mathbf{y}_0-\mathbf{x}_2}\cdot\mathbf{v}_0/c_0}{1+\widehat{\mathbf{y}_0-\mathbf{x}_1}\cdot\mathbf{v}_0/c_0}=\gamma_{\boldsymbol{y}_0,\boldsymbol{v}_0,21}\,. \quad (39)$$

Note that $\mathbf{y}_0=(\boldsymbol{y}_0,h)$ and $\mathbf{v}_0=(\boldsymbol{v}_0,0)$. Under the slower-mover assumption, $\gamma_{\boldsymbol{y},\boldsymbol{v},ij}$ can be approximated as follows:

$$\gamma_{\boldsymbol{y},\boldsymbol{v},ij}=\frac{1+\widehat{\mathbf{y}-\mathbf{x}_i}\cdot\mathbf{v}/c_0}{1+\widehat{\mathbf{y}-\mathbf{x}_j}\cdot\mathbf{v}/c_0}\approx 1+(\widehat{\mathbf{y}-\mathbf{x}_i}-\widehat{\mathbf{y}-\mathbf{x}_j})\cdot\mathbf{v}/c_0\,. \quad (40)$$

Let

$$\{(\boldsymbol{y},\boldsymbol{v})\in\mathbb{R}^2\times\mathbb{R}^2:\gamma_{\boldsymbol{y},\boldsymbol{v},ij}=C\} \quad (41)$$

for some constant $C\in\mathbb{R}^+$. Using (40), $\gamma_{\boldsymbol{y},\boldsymbol{v},ij}=C$ can be written as

$$(\widehat{\mathbf{y}-\mathbf{x}_2}-\widehat{\mathbf{y}-\mathbf{x}_1})\cdot\mathbf{v}=(C-1)c_0\,. \quad (42)$$

Note that if we multiply both sides by ω, the left-hand side of (42) becomes the *hitchhiker-Doppler* defined in [13]. In this regard, we refer to the four-dimensional manifold formed by $\{(\boldsymbol{y},\boldsymbol{v})\in\mathbb{R}^2\times\mathbb{R}^2:\gamma_{\boldsymbol{y},\boldsymbol{v},ij}=C\}$ in $(\boldsymbol{y},\boldsymbol{v})$ space, for some constant $C\in\mathbb{R}^+$, as a *passive-iso-Doppler manifold*.

Thus, (39) specifies a passive-iso-Doppler manifold with respect to two receivers located at $\mathbf{x}_1$ and $\mathbf{x}_2$. The test-statistic due to a moving point target located at $\boldsymbol{y}_0$ moving with velocity $\boldsymbol{v}_0$ is constant on this mainfold.

Substituting (39) into the left-hand side of (38), we obtain

$$|\mathbf{y}-\mathbf{x}_2|-\gamma_{\boldsymbol{y},\boldsymbol{v},21}|\mathbf{y}-\mathbf{x}_1|=|\mathbf{y}_0-\mathbf{x}_2|-\gamma_{\boldsymbol{y}_0,\boldsymbol{v}_0,21}|\mathbf{y}_0-\mathbf{x}_1|\,. \quad (43)$$

Let

$$r_{21}(\boldsymbol{y},\boldsymbol{v})=|\mathbf{y}-\mathbf{x}_2|-\gamma_{\boldsymbol{y},\boldsymbol{v},21}|\mathbf{y}-\mathbf{x}_1|\,. \quad (44)$$

We refer to $r_{21}(\boldsymbol{y},\boldsymbol{v})$ as *passive-range*. For a pair of receivers located at $\mathbf{x}_1$ and $\mathbf{x}_2$, $\{(\boldsymbol{y},\boldsymbol{v})\in\mathbb{R}^2\times\mathbb{R}^2:r_{12}(\boldsymbol{v},\boldsymbol{y})=C\}$ where $C\in\mathbb{R}^+$ denotes some constant forms a manifold in the four-dimensional $(\boldsymbol{y},\boldsymbol{v})$ space. We refer to the this manifold as a *passive-iso-range manifold*. (43) specifies a passive-iso-range manifold with respect to two receivers located at $\mathbf{x}_1$ and $\mathbf{x}_2$. The test-statistic due to a moving point target located at $\boldsymbol{y}_0$ moving with velocity $\boldsymbol{v}_0$ is constant on this manifold.

Based on the analysis above, we conclude that PSF peaks at the intersection of the passive-iso-Doppler manifold defined by (39), and the passive-iso-range manifold defined by (43). Note that (37) can be interpreted as a generalized auto-ambiguity function of the transmitted waveform p_1. The spread of the passive-iso-Doppler manifold and the passive-iso-range manifold are both related to the shape of this generalized auto-ambiguity function. Hence, the resolution of the reconstructed image in $(\boldsymbol{y},\boldsymbol{v})$ is determined by the overlapping area between the passive-iso-Doppler and passive-iso-range manifolds.

For $N>2$ receivers, it can be shown that multiple pairs of receivers generate multiple four-dimensional passive-iso-Doppler and passive-iso-range manifolds. These manifolds intersect at the correct target location and correct velocity in $(\boldsymbol{y},\boldsymbol{v})$ space and contribute to the reconstruction of the target image. The test-statistic value at the the correct target location and correct velocity increases by roughly a factor of $N-1$ as compared to the two-receiver scenario as described in (34).

In order to be able to visualize the four-dimensional PSF and to gain insight into passive range and velocity resolutions, we consider the cross-sections of the passive-iso-Doppler and passive-iso-range manifolds for constant position and constant velocity. Under the slow-mover assumption, (39) becomes

$$(\widehat{\mathbf{y}-\mathbf{x}_2}-\widehat{\mathbf{y}-\mathbf{x}_1})\cdot\mathbf{v}=(\widehat{\mathbf{y}_0-\mathbf{x}_2}-\widehat{\mathbf{y}_0-\mathbf{x}_1})\cdot\mathbf{v}_0. \quad (45)$$

Using (45), we define

$$F_{\boldsymbol{v}_0,21}(C)=\{\boldsymbol{y}\in\mathbb{R}^2:(\widehat{\mathbf{y}-\mathbf{x}_2}-\widehat{\mathbf{y}-\mathbf{x}_1})\cdot\mathbf{v}_0 =(\widehat{\mathbf{y}_0-\mathbf{x}_2}-\widehat{\mathbf{y}_0-\mathbf{x}_1})\cdot\mathbf{v}_0\} \quad (46)$$

and

$$F_{\boldsymbol{y}_0,21}(C)=\{\boldsymbol{v}\in\mathbb{R}^2:(\widehat{\mathbf{y}_0-\mathbf{x}_2}-\widehat{\mathbf{y}_0-\mathbf{x}_1})\cdot\mathbf{v} =(\widehat{\mathbf{y}_0-\mathbf{x}_2}-\widehat{\mathbf{y}_0-\mathbf{x}_1})\cdot\mathbf{v}_0\ \}. \quad (47)$$

For a pair of receivers located at $\mathbf{x}_1$ and $\mathbf{x}_2$ and target velocity $\boldsymbol{v}_0$, (46) specifies a passive-iso-Doppler curve in the two-dimensional position space. We refer to this curve as the *position-related passive-iso-Doppler contour*. Similarly, for a pair of receivers located at $\mathbf{x}_1$ and $\mathbf{x}_2$ and a target located at $\boldsymbol{y}_0$, (47) specifies a passive-iso-Doppler curve in the two-dimensional velocity space. We refer to this curve as the *velocity-related passive-iso-Doppler contour*.

Let ϕ_{12} be the angle between $\widehat{\mathbf{y}_0-\mathbf{x}_1}$ and $\widehat{\mathbf{y}_0-\mathbf{x}_2}$ and θ (θ_0) be the angle between $\boldsymbol{v}$ ($\boldsymbol{v}_0$) and $\widehat{\mathbf{y}_0-\mathbf{x}_2}-\widehat{\mathbf{y}_0-\mathbf{x}_1}$. Then, (47) can be expressed as

$$\begin{aligned}&2\sin\left(\tfrac{\phi_{12}}{2}\right)|\boldsymbol{v}|\cos\theta=2\sin\left(\tfrac{\phi_{12}}{2}\right)|\boldsymbol{v}_0|\cos\theta_0\\ \Rightarrow\quad&|\boldsymbol{v}|\cos\theta=|\boldsymbol{v}_0|\cos\theta_0\,.\end{aligned} \quad (48)$$

It can be seen that the velocity-related passive-iso-Doppler contour, specified by (47) and (48), corresponds to a line on the velocity plane that is perpendicular to the vector $\widehat{\mathbf{y}_0-\mathbf{x}_2}-\widehat{\mathbf{y}_0-\mathbf{x}_1}$ with its distance to the origin being $|\boldsymbol{v}_0|\cos\theta_0$.

Similarly, we consider the cross-sections of the passive iso-range manifold given in (43) for a constant velocity, $\boldsymbol{v}_0$ and a

constant position $\boldsymbol{y}_0$:

$$R_{\boldsymbol{v}_0,21}(C) = \{\boldsymbol{y} \in \mathbb{R}^2 : |\mathbf{y}-\mathbf{x}_2| - \gamma_{\boldsymbol{y},\boldsymbol{v}_0,21}|\mathbf{y}-\mathbf{x}_1| = |\mathbf{y}_0-\mathbf{x}_2| - \gamma_{\boldsymbol{y}_0,\boldsymbol{v}_0,21}|\mathbf{y}_0-\mathbf{x}_1|\} \quad (49)$$

and

$$R_{\boldsymbol{y}_0,21}(C) = \{\boldsymbol{v} \in \mathbb{R}^2 : |\mathbf{y}_0-\mathbf{x}_2| - \gamma_{\boldsymbol{y}_0,\boldsymbol{v},21}|\mathbf{y}_0-\mathbf{x}_1| = |\mathbf{y}_0-\mathbf{x}_2| - \gamma_{\boldsymbol{y}_0,\boldsymbol{v}_0,21}|\mathbf{y}_0-\mathbf{x}_1|\}. \quad (50)$$

Note that under the slow-mover approximation given in (40), (50) reduces to (47). We refer to (49) as the *position-related passive-iso-range contour*. Since under the slow-mover assumption $\gamma_{\boldsymbol{y},\boldsymbol{v},21}$ is close to 1, we see that the position-related passive-iso-range contours are similar to the hyperbolas with their foci located at $\mathbf{x}_1$ and $\mathbf{x}_2$.

From the analysis above, we conclude that the velocity resolution is related to the spread of the velocity-related passive-iso-Doppler contours. The position resolution may be related to the spread of the position-related passive-iso-Doppler contour or position-related passive-iso-range contour, depending on the Doppler and range ambiguities of the transmitted waveform: If the transmitted waveform has good Doppler resolution, but poor range resolution, the position resolution primarily depends on the spread of the position-related passive-iso-Doppler contours. If, on the other hand, the transmitted waveform has only good range resolution, the position reconstruction primarily depends on the spread of the position-related passive-iso-range contours.

Note that if the transmitted waveform has both good Doppler and good range resolution, the position resolution depends on the cross-section of the intersection of the passive-iso-Doppler and passive-iso-range manifolds for constant velocity, which is neither the position-related passive-iso-Doppler contours nor the position-related passive-iso-range contours. However, this cross-section becomes one of the two types of the contours described above as the range or Doppler resolution of the waveform degrades or improves.

V. Numerical Simulations

We conducted numerical simulations to demonstrate the performance of our passive imaging method using a moving point target model.

We considered a scene of size $[0, 3\text{e}3] \times [0, 3\text{e}3]\,\text{m}^2$ with flat topography. We discretized the scene into 201×201 pixels where $[0, 0, 0]\,\text{m}$ and $[3\text{e}3, 3\text{e}3, 0]\,\text{m}$ correspond to the pixels $(1, 1)$ and $(201, 201)$, respectively. We assumed that the target velocity is in the range of $[-20, 20] \times [-20, 20]\,\text{m/s}$. We discretized the velocity plane into 401×401 pixels where $[-20, -20, 0]\,\text{m}$ and $[20, 20, 0]\,\text{m}$ correspond to the pixels $(1, 1)$ and $(401, 401)$, respectively. The point target with unit reflectivity was assumed to be located at $[2.5\text{e}3 \quad 2\text{e}3 \quad 0]^T\,\text{m}$ moving with velocity $[-10, 15]\,\text{m/s}$.

We assumed that there was a single transmitter and ten receivers present in the scene. The single transmitter was assumed to be located at $[1.5\text{e}3, 0, 6]^T\,\text{m}$. The receivers were evenly distributed around the scene.

We considered two types of transmitted waveforms in our simulations: The first type of waveforms have high Doppler resolution and relatively poor range resolution, such as Frequency Modulated (FM) radio and television signals, etc. We refer to such waveforms as the high-Doppler resolution waveforms. We simulated a high-Doppler resolution waveform as a single-frequency continuous-wave (CW) with 4GHz carrier frequency and 0.1s duration in our experiments. Such a waveform provides a radial velocity resolution of about $0.375\,\text{m/s}$ for monostatic operations. The second type of waveforms, we considered, have not only good Doppler resolution, but also acceptable range resolution. Examples for such waveforms include wireless network (or WiFi) signals and WiMAX waveforms which have relatively large bandwidth that can offer reasonable range resolution. We refer to such waveforms as the high-Doppler and good-range resolution waveforms. We simulated a high-Doppler and good-range resolution waveform with the same carrier frequency and duration as the high-Doppler resolution waveform, but with an additional frequency modulation, which results in a bandwidth of 7.5MHz. Such a waveform provides about $19.5\,\text{m}$ range resolution, and $0.375\,\text{m/s}$ radial velocity resolution in monostatic operations.

In all the experiments, we simulated the thermal noise as an additive white Gaussian process.

We reconstructed the four-dimensional test-statistic image in $(\boldsymbol{y}, \boldsymbol{v})$ (or (y_1, y_2, v_1, v_2)) coordinates. However, in order to facilitate visualization and performance evaluation, we generated three two-dimensional images from the original four dimensional image: The fist image, which we refer to as the peak-value image, was generated by choosing the maximum value of the four-dimensional image for each velocity (v_1, v_2). We then, choose the maximum value, $\tilde{\boldsymbol{v}}$, of the peak-value image as the estimate of the velocity. The second image, which we refer to as the position-image, is the cross-section of the four-dimensional image, for $\boldsymbol{v} = \tilde{\boldsymbol{v}}$. We take the maximum value, $\tilde{\boldsymbol{y}}$, of the position-image as the estimate of the target's position. The third image, which we refer to as the velocity-image, is the cross-section of the four-dimensional image, for $\boldsymbol{y} = \tilde{\boldsymbol{y}}$. We performed the performance evaluation using the position- and velocity-images.

The reconstructed images of the moving point target using the high-Doppler resolution waveform and high-Doppler and good-range resolution waveform are shown in Fig. 1 and Fig. 2, respectively. The maximum value of the peak-value image, which corresponds to the estimated velocity, $\tilde{\boldsymbol{v}}$, is indicated by a circle. The true position of the target is indicated by a solid red dot. The true velocity is indicated by a solid blue dot.

We see that the target location and velocity can be reconstructed correctly in both cases. In the case where a high-Doppler resolution waveform is used, the position-image is the superposition of the position-related passive-iso-Doppler curves that intersect at the correct target location, as shown in Fig. 1(b). The velocity-image, as shown in Fig. 1(c), is the sum of the velocity-related passive-iso-Doppler contours formed by each pair of receivers. Note that the velocity-related

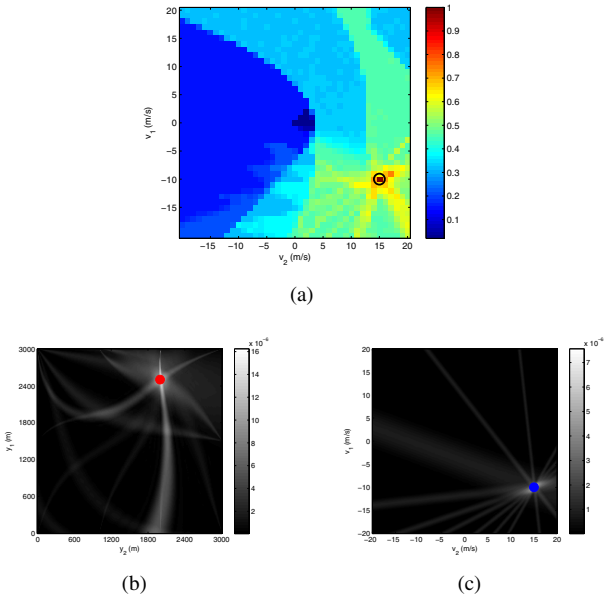

(a)

(b) (c)

Fig. 1. The reconstructed images for a moving point target with 10 receivers and a single transmitter transmitting a high-Doppler resolution waveform: (a) The peak-value image with the maximum value indicated by a circle. The estimated velocity $\tilde{\boldsymbol{v}} = (-10, 15)\mathrm{m/s}$. (b) The position-image when $\boldsymbol{v} = \tilde{\boldsymbol{v}}$. The estimated position $\tilde{\boldsymbol{y}} = (2500, 2000)\mathrm{m}$. (c) The velocity-image when $\boldsymbol{y} = \tilde{\boldsymbol{y}}$. Solid dots indicate the true position (or velocity).

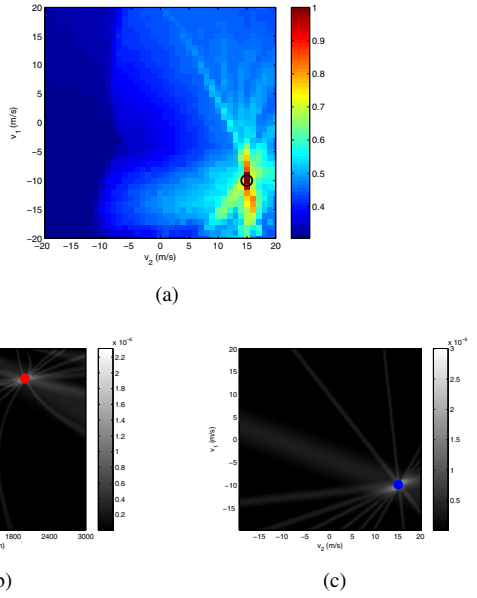

(a)

(b) (c)

Fig. 2. The reconstructed images for a moving point target with 10 receivers and a single transmitter transmitting a high-Doppler and good-range resolution waveform: (a) The peak-value image with the maximum value indicated by a circle. The estimated velocity $\tilde{\boldsymbol{v}} = (-10, 15)\mathrm{m/s}$. (b) The position-image with $\boldsymbol{v} = \tilde{\boldsymbol{v}}$. The estimated position $\tilde{\boldsymbol{y}} = (2500, 2000)\mathrm{m}$. (c) The velocity-image with $\boldsymbol{y} = \tilde{\boldsymbol{y}}$. Solid dots indicate the true position (or velocity).

passive-iso-Doppler contours are straight lines as described in Section IV.

We observe that the velocity estimates obtained using the two different waveforms are almost the same when Fig. 2(c) is compared with Fig. 1(c). This is consistent with our analysis in Section IV, which states that the velocity resolution depends only on the Doppler ambiguity of the transmitted waveform. Furthermore, comparing Fig. 2(b) with Fig. 1(b), we observe that the position-images obtained using the high-Doppler and good-range resolution waveform are not simply the sum of the position-related passive-iso-Doppler curves due to the good range ambiguity provided by the waveform. For this type of waveforms, multiple passive-iso-range manifolds along with multiple passive-iso-Doppler manifolds contribute to the intersection at the correct target position. As a result, the projection of the intersection onto the position plane is no longer simply the position-related passive-iso-Doppler or the position-related passive-iso-range curves as can be observed in Fig. 2(b).

VI. Conclusion

In this work, we developed a new passive radar imaging method for moving targets using sparsely distributed receivers. We analyzed the resolution of our passive imaging method and demonstrated its performance in numerical simulations. While we mainly focused on passive radar application, the results presented in our paper are also applicable to other wave-based passive imaging applications, such as passive acoustic or seismic imaging.

References

[1] H. D. Griffiths and C. J. Baker, "Passive coherent location radar systems. part 1: Performance prediction," *IEE Proceedings of Radar, Sonar and Navigation*, vol. 152, no. 3, pp. 153–159, June 2005.

[2] D. W. O'Hagan and C. J. Baker, "Passive bistatic radar (PBR) using FM radio illuminators of opportunity," in *Proc. of 2008 IEEE Radar Conference, Roma, Italy*, May 2008.

[3] D. Poullin, "Passive detection using digital broadcasters (DAB, DVB) with COFDM modulation," *IEE Proceedings of Radar, Sonar and Navigation*, vol. 152, no. 3, pp. 143–152, June 2005.

[4] D. K. P. Tan, H. Sun, Y. Lu, M. Lesturgie, and H. L. Chan, "Passive radar using global system for mobile communication signal: theory, implementation and measurements," *IEE Proceedings of Radar, Sonar, and Navigation*, vol. 152, no. 3, pp. 116–123, June 2005.

[5] P. E. Howland, D. Maksimiuk, and G. Reitsma, "Fm radio based bistatic radar," *IEE Proceedings of Radar, Sonar and Navigation*, vol. 152, no. 3, pp. 107–115, June 2005.

[6] K. S. Kulpa, "Multi-static entirely passive detection of moving targets and its limitations," *IEE Proceedings of Radar, Sonar, and Navigation*, vol. 152, no. 3, pp. 169–173, June 2005.

[7] C. Coleman and H. Yardley, "Passive bistatic radar based on target illumniations by digital audio broadcasting," *IET Radar Sonar Navig.*, vol. 2, no. 5, pp. 366–375, 2008.

[8] K. Chetty, K. Woodbridge, H. Guo, and G. E. Smith, "Passive bistatic WiMAX radar for marine surveillance," in *Proc. of 2010 IEEE Radar Conference, Washington, DC, USA*, May 2010.

[9] P. Falcone, F. Colone, C. Bongioanni, and P. Lombardo, "Experimental results for OFDM WiFi-based passive bistatic radar," in *Proc. of 2010 IEEE Radar Conference, Washington, DC, USA*, May 2010.

[10] Y. Wu and D. C. Munson, "Multistatic synthetic aperture imaging of aircraft using reflecting television signals," in *Proc. of SPIE, Algorithms for Synthetic Aperture Radar Imagery VIII*, April 2001.

[11] M. Cheney and B. Borden, "Imaging moving targets from scattered waves," *Inverse Problems*, vol. 24, pp. 035 005(1–22), 2008.

[12] S. M. Kay, *Fundamentals of Statistical Signal Processing, Vol. I and Vol. II*. Prentice Hall, 1998.

[13] C. E. Yarman and B. Yazıcı, "Synthetic aperture hitchhiker imaging," *IEEE Transactions on Imaging Processing*, vol. 17, no. 11, pp. 2156–2173, November 2008.